Scripta Materialia 158 (2019) 105–109

Contents lists available at ScienceDirect

Scripta Materialia

journal homepage: www.elsevier.com/locate/scriptamat

Regular Article

Multi-scale analyses of constituent phases in a trip-assisted duplex stainless steel by electron backscatter diffraction, in situ neutron diffraction, and energy selective neutron imaging

Wanchuck Woo [a,*], Jongyul Kim [a], Eun-Young Kim [b], Shi-Hoon Choi [b], Vyacheslav Em [c], Daniel S. Hussey [d]

[a] Neutron Science Center, Korea Atomic Energy Research Institute, Daejeon 34057, South Korea
[b] Department of Printed Electronics Engineering, Sunchon National University, Sunchon 57922, South Korea
[c] Neutron Research Department, NRC Kurchatov Institute, Moscow, Russian Federation
[d] Physical Measurement Laboratory, NIST, Gaithersburg, MD 20899, USA

ARTICLE INFO

Article history:
Received 24 May 2018
Received in revised form 30 July 2018
Accepted 22 August 2018
Available online 2 September 2018

Keywords:
Volume fractions
Trip-assisted duplex stainless steel
Electron backscatter diffraction
In situ neutron diffraction
Energy selective neutron imaging

ABSTRACT

Micrometer to centimeter scale analyses of the crystalline phase volume fractions in a trip-assisted duplex stainless steel were performed under loading using electron backscatter diffraction (EBSD), in situ neutron diffraction, and energy selective neutron imaging (ESNI) methods. In contrast to the localized investigations of EBSD, ESNI provides macroscopic spatial distributions in a volume-averaged manner over the entire specimen with a spatial resolution of about 65 μm. The ESNI shows that the martensite is concentrated on the necking region and estimates its volume fraction of 14% at a strain of 0.2, which is comparable to the neutron diffraction result.

Duplex stainless steels (DSS) typically contain higher chromium and lower nickel chemical compositions (for example, 24Cr-4Ni) compared to the austenitic stainless steels (18Cr-10Ni) and consist of a two-phase microstructure, namely the fcc-γ austenite phase in bcc-α ferrite matrix, to provide an excellent combination of strength and ductility and robust resistance to stress corrosion cracking [1]. A number of strategic alloy designs, so-called "lean DSS", have been reported to enhance the strength and corrosion properties by replacing the expensive Ni and Mo alloys with Mn and N components with the benefits of solid solution strengthening and resistance to local corrosion/sensitization mechanisms [2–11].

More attention has been recently focused on the phase stability of the metastable austenite phase (fcc, γ) within the DSS, because it can generate the beneficial transformation-induced plasticity (TRIP) phenomenon under deformation (termed TRIP-assisted DSS) [3,7–11]. The higher concentration of Mn and N and lower Ni concentration in the austenite phase can decrease the stacking fault energy reported ~22 mJ/m^2 so that the martensite (bct-α′ or hcp-ε) phase formation can be activated under deformation [7,11]. Thus, an accurate determination of the metastable phase and its volume fraction is essential to elucidate the microstructure, mechanical properties, and physical simulation schemes [8,10]. Up to date, the evolutions of the constituent phases have been widely examined by using electron backscatter diffraction (EBSD) [3,9,11], magnetization method [10], x-ray diffraction [6,9], and neutron diffraction [8].

Those methods are, however, inherently constrained to localized scanning sizes of the specimen, for example, up to a few hundred micrometers scale in the case of the EBSD/x-ray diffraction and a few millimeters of the neutron diffraction techniques. In this regard, energy selective neutron imaging (ESNI) method was applied to provide the macroscopic phase distributions of the entire specimen [12–20]. The purpose of this paper is to examine the volume fractions of phases as a function of strain in a TRIP-assisted DSS by using EBSD, in situ neutron diffraction, and ESNI methods. Comparison among the three kinds of results can overcome the critical limitations of the localized sampling size issue and highlight the macroscopic centimeter-scale features through the whole specimen.

As-received TRIP-assisted DSS has a nominal chemical composition of 0.03C-0.6Si-1.8Mn-21.9Cr-2.5Ni-0.6Mo-0.5Cu-0.17N-bal. Fe (wt%). The initial constituent phases of ferrite (bcc, α) and austenite (fcc, γ) mainly involves a direct γ transformation to martensite (hcp, α′) via the TRIP phenomenon under deformation (γ → α′). The total of five plate type tensile specimens were prepared using electrical discharge machining with a total length of 100 mm and a parallel gauge length of 25 mm. The width and thickness of the gauge length part of the sample were 3 mm and 1.6 mm, respectively. Four specimens were tensile loaded separately up to the true strain (ε) of 0, 0.1, 0.15, and 0.2 with

* Corresponding author.
E-mail address: chuckwoo@kaeri.re.kr (W. Woo).

https://doi.org/10.1016/j.scriptamat.2018.08.040
1359-6462/

the strain rate of 1.0×10^{-3} s^{-1}. Each specimen was used for the EBSD and ESNI experimental analyses. One specimen was used for the in-situ neutron diffraction experiment under tensile loading. The true yield strength was 590 MPa and true tensile strength was 830 MPa at $\varepsilon = 0.2$.

The constituent phases of the TRIP-assisted DSS specimen were analyzed by EBSD of a field emission scanning electron microscopy. The EBSD samples were taken at the mid-length, prepared by standard polishing procedures, and the phase volume fractions were averaged by measuring at the cross-sections along the rolling (x), transverse (y), and normal (z) directions of the specimen in the center parts through the thickness direction, respectively. The dimensions of the measurement step and the scan area were 0.5 μm and 300 × 300 μm^2, respectively. It is important to note that the average volume fractions were 65% of the α and 35% of the γ phase along the three directions in the initial state ($\varepsilon = 0$), which is typically reported in the TRIP DSS specimen [8]. Meanwhile, for an arbitrarily selected region (47.5 μm × 44.9 μm) of the EBSD method, it can provide the composition of about 5% of the α and 95% of the γ phases initially, as shown in Fig. 1(a). Fig. 1 (b)–(d) show that the volume fraction of the α+α′ increases from 0.12 to 0.35 while the γ decreases from 0.88 to 0.65 as straining from 0.1 to 0.2.

In-situ neutron diffraction experiments were performed during uniaxial tension to measure the evolution of the peak intensities in (hkl) planes. The peak intensities can be used to calculate the volume fraction of the constituent phases in the TRIP-assisted DSS. These experiments were conducted using the Residual Stress Instrument at the Korea Atomic Energy Research Institute [21]. The specimen was installed on the load flame with the gauge length parallel to the loading direction (Q-vector//x), as shown in Fig. 2(a). Neutron beam with a wavelength (λ) of 1.46 Å provides (211) and (311) diffraction peaks for the α/α′ and γ phase analyses at the diffraction angles (2θ) of 76.2° and 83.6°, respectively. The scattering gauge volume defined by neutron beam slits was about 5 (x) × 2 (y) × 1.6 (z) mm^3. The strain rate was kept as 1.0×10^{-3} s^{-1} and the diffraction peaks were measured for 10 min at each static stage of the strain (ε) of 0, 0.1, 0.15, and 0.2 under the tensile loading.

Fig. 2 shows the diffraction peaks of (211) and (311) at the strain of 0.2. Those peaks were selected because of the preferred orientation anisotropy via large multiplicity factors in a polycrystalline material [22]. The peak separation between the martensite (bct, α′) and ferrite (bcc, α) phases was available from the distinct asymmetric broadening due to the different elastic constants of the two structures under loading as shown in Fig. 2(b) [21]. Note that the volume fraction of the constituent phases was analyzed by the integrated intensity of the Gaussian peak fitting. Assume that the specimen consists of two phases (α′ and γ) with the constant ferrite volume fraction (V_α), then the relationship between integrated intensity (I) and volume fraction (V) of two phases (α′ and γ) is given as [22]:

$$\frac{I_\gamma}{I_{\alpha'}} = \left(\frac{V_\gamma}{V_{\alpha'}}\right)\left[\left(\frac{jN_C^2F^2}{\sin\theta\,\sin 2\theta}\right)_\gamma \Big/ \left(\frac{jN_C^2F^2}{\sin\theta\,\sin 2\theta}\right)_{\alpha'}\right] = \left(\frac{V_\gamma}{V_{\alpha'}}\right)K \quad (1)$$

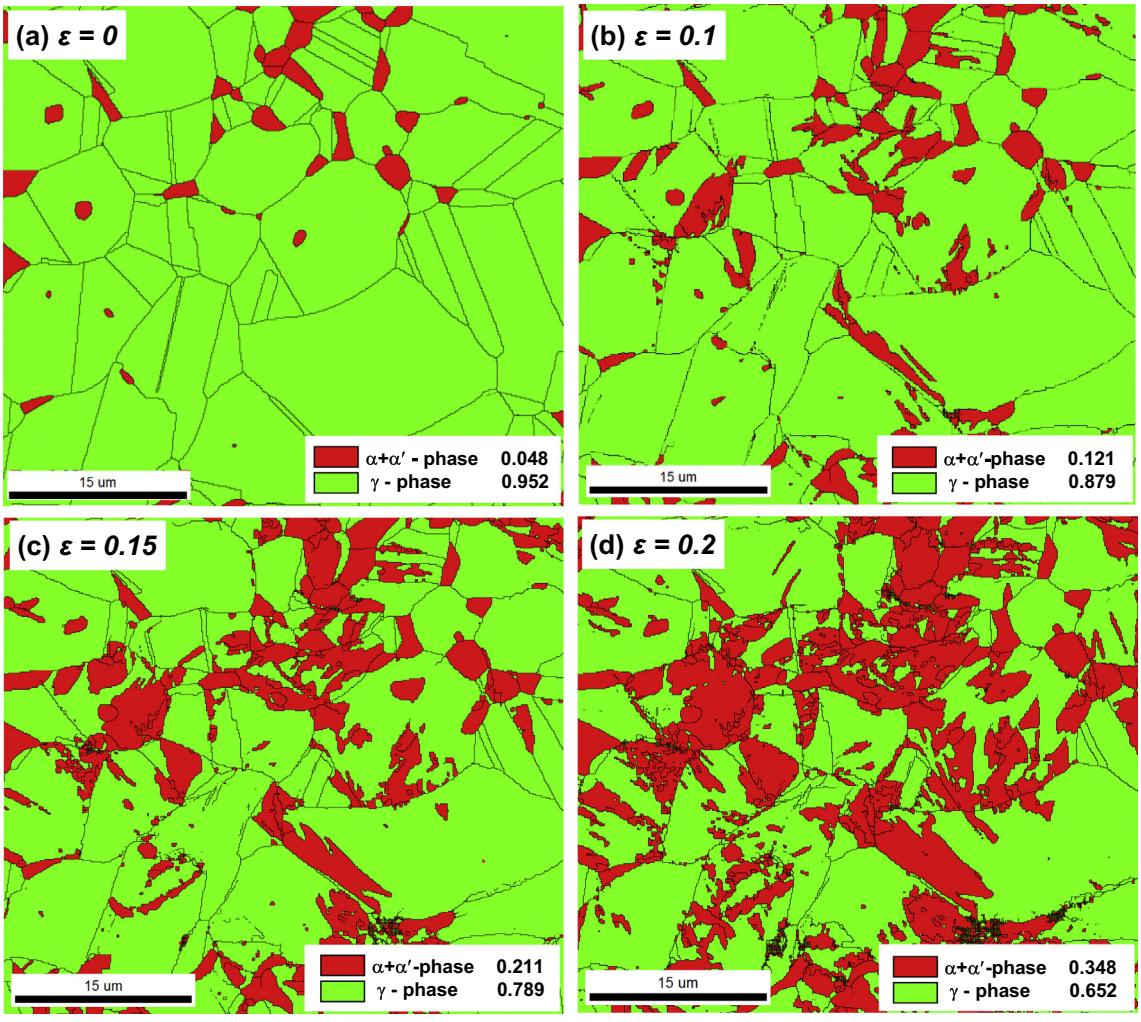

Fig. 1. EBSD analyses at the strain (ε) of (a) 0, (b) 0.1, (c) 0.15, and (d) 0.2 in a trip-assisted duplex stainless steel. Denoted phase volume fractions of the ferrite (bcc, α), martensite (hcp, α′), and austenite (fcc, γ) analyzed from an arbitrarily selected location of the specimen.

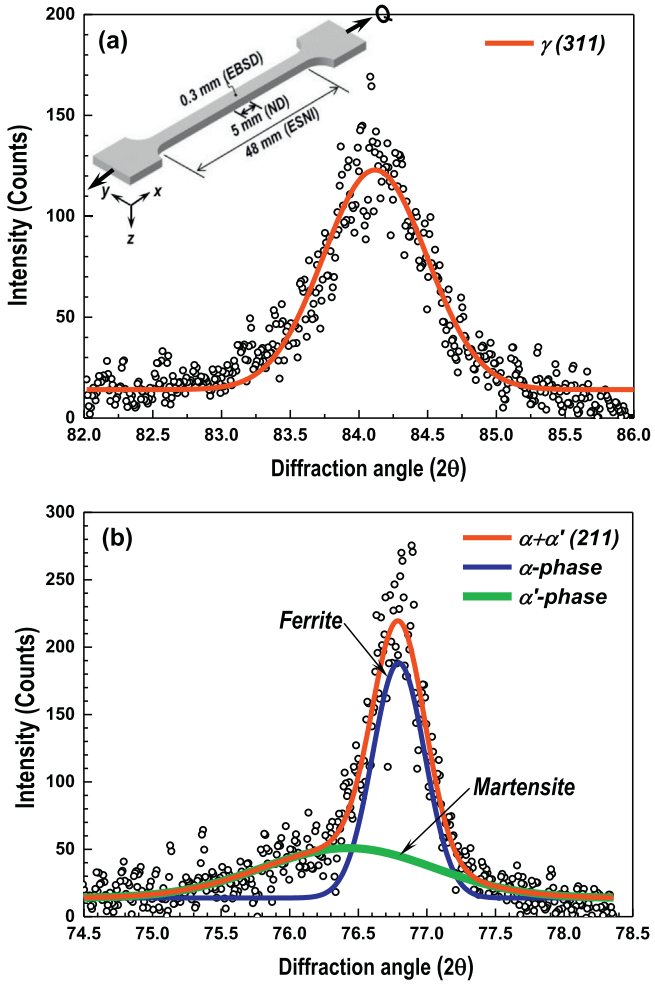

Fig. 2. Neutron diffraction peaks at the strain (ε) of 0.2: (a) (311) austenitic peak (fcc, γ) and (b) (211) diffraction peak. The (211) peak convoluted ferrite (bcc, α) and martensite (hcp, α′) phases was fitted using two-peak Gaussian fitting method. The inset of (a) is the shape of specimen and sketched the scan sizes of EBSD, neutron diffraction (ND), and energy selective neutron imaging (ESNI).

where j is the multiplicity factor ($j_{\gamma}^{311} = 24$, $j_{\alpha'}^{211} = 24$), N_c is the number of unit cells per cm^3 ($N_c = a^3$, a is the lattice parameter, $a_{\gamma} = 3.608 \times 10^{-8}$ cm, $a_{\alpha'} = 2.860 \times 10^{-8}$ cm), F is the structure factor per unit cell ($F_{\gamma}^{311} = 4b_{avg}$, $F_{\alpha'}^{211} = 2b_{avg}$, the b_{avg} is the average scattering length, which is the same for phases). Thus, one obtains $K = 0.921$. If we let $V_{\gamma}/V_{\alpha'} = (I_{\gamma}/I_{\alpha'})/K = \beta$, $V_{\alpha} + V_{\alpha'} + V_{\gamma} = 1$ leads the volume fraction of martensite phase, $V_{\alpha'} = \beta\,(1 - V_{\alpha})/(1 + \beta)$. In this regard, the volume fractions of the constituent phases in each strain stage were determined from the diffraction peaks and the results were summarized in Table 1.

Table 1
Volume fractions of ferrite (bcc, α), martensite (hcp, α′), and austenite (fcc, γ) as a function of true strain (ε) in a trip-assisted duplex stainless steel analyzed by electron backscatter diffraction (EBSD), in situ neutron diffraction, and energy selective neutron imaging (ESNI). Note that EBSD is obtained from an arbitrarily selected location of the specimen.

Strain (ε)	EBSD		Neutron			Imaging		
	α + α′	γ	α + α′	γ	α′	α + α′	γ	α′
0	0.05	0.95	0.63	0.37	0.00	0.58	0.42	0.00
0.10	0.12	0.88	0.67	0.33	0.04	0.66	0.34	0.08
0.15	0.21	0.79	0.74	0.26	0.11	0.70	0.30	0.12
0.20	0.35	0.65	0.79	0.21	0.16	0.72	0.28	0.14

Fig. 3(a) shows the total neutron cross-section (σ) of the bcc ferrite and fcc austenite steels as a function of λ calculated by equations of the scattering theory [23]. The neutron cross-section, which is defined as the scattering event rates between nucleus and neutrons, abruptly changes in the vicinity of the individual (hkl) lattice planes when satisfying $\lambda = 2d_{hkl}$, where d_{hkl} is the interplanar spacing between hkl lattice planes. Since these lattice planes no longer contribute to Bragg scattering for $\lambda > 2d_{hkl}$, most neutrons are transmitted and this increase is referred to as Bragg edge. Here, we select a particular wavelength (λ_1) of 4.1 Å, where the σ of the bcc (110) is significantly lower than that of the fcc (111) as shown in Fig. 3(a). Thus, the energy selected neutron beam can significantly increase its penetration with low attenuation for bcc (bct is the same) compared to the fcc structure and it results in a remarkably clear image contrast between the bcc and fcc phases in crystalline materials.

The imaging experiments were performed at the NG-6 cold neutron imaging instrument (CNII) at National Institute of Standards and Technology (NIST) [19]. A double crystal monochromator made of a highly oriented pyrolytic graphite was installed for (002) reflections and the transmission intensity changes were measured in the range of 2.2 Å to 4.3 Å with a resolution ($\Delta\lambda/\lambda$) of about 3%. A 300 μm-thick LiF-ZnS neutron scintillator and lens coupled camera detector were utilized. Fig. 3 (b) shows the variations of the transmission intensities for the bcc phase as a function of λ. It shows the transmission intensity is low when $\varepsilon = 0$ compared to the strain of $\varepsilon = 0.2$. The difference is maximized at the λ_1 of 4.1 Å. Thus, using the wavelength, a total of nine images were taken, median filtered, and averaged from the scanning window with the size of 48 (x) × 3 (y) × 1.6 (z) mm^3 as a marked square in Fig. 3(c). It should be mentioned that the transmission intensity data were divided (4.1 Å/4.3 Å) individually to normalize and eliminate any possible background influence and material inhomogeneities in each location.

The transmission intensity data from the ESNI can be transformed to the volume fractions of the constituent phases in the TRIP-assisted DSS specimens. The attenuation of neutron transmission intensity (I) is given by $I = I_o \exp(-\mu t)$, where the I_o is the incident neutron flux, the μ is the attenuation coefficient ($\mu = n \cdot \sigma$, the n is the number density), and t is the sample thickness [14,23]. Thus, the phase volume fraction (V) can be related to the measured transmission intensity ratio (A);

$$\frac{\mu_{4.1}}{\mu_{4.3}} = \frac{\ln(I_o/I_{4.1})}{\ln(I_o/I_{4.3})} = \frac{V\sigma_{4.1}^{bcc} + (1-V)\sigma_{4.1}^{fcc}}{\sigma_{4.3}} = A;\ V = \frac{A\sigma_{4.3} - \sigma_{4.1}^{fcc}}{\left(\sigma_{4.1}^{bcc} - \sigma_{4.1}^{fcc}\right)}; \quad (2)$$

where the μ_i is the attenuation at a wavelength (i) and the σ_i is the total neutron cross-section at a wavelength for each phase. As a result, Fig. 3 (c)–(f) show the distribution of the bcc/bct phase volume fraction as a function of strain. Assuming no martensite (α′) at $\varepsilon = 0$, Fig. 3(c), the initial volume fraction was analyzed as 0.58 for the ferrite (bcc, α) and 0.42 for the austenite (fcc, γ) by indexing of the imaging pixel data at each location. Table 1 compares the imaging results with the other methods. The sum of α and α′ volume fraction increases from 0.58 to 0.72 whereas the γ decreases from 0.42 to 0.28 with applied strain. Assuming no martensite (α′) initially, it shows that the volume fraction of the α′ is 0.14 at a strain of 0.2.

Fig. 4 compares the volume fraction changes as a function of strain analyzed by the three different methods (EBSD, neutron diffraction, and ESNI). The EBSD is suitable and important for the qualitative analysis though, the volume fraction can lead to be misleading due to an arbitrary selection of the localized region for investigation. Indeed, one can select a location (0.3 mm scanning size) having the volume fraction of 0.95 for γ and 0.05 for α as shown in Fig. 1(a), even though the typical volume fraction is known as about 0.35 for γ and 0.65 for α initially [8]. Thus, significant discrepancies are shown in Fig. 4 between EBSD and neutron diffraction/imaging results. A modified analysis of the EBSD result ($EBSD^M$) can be

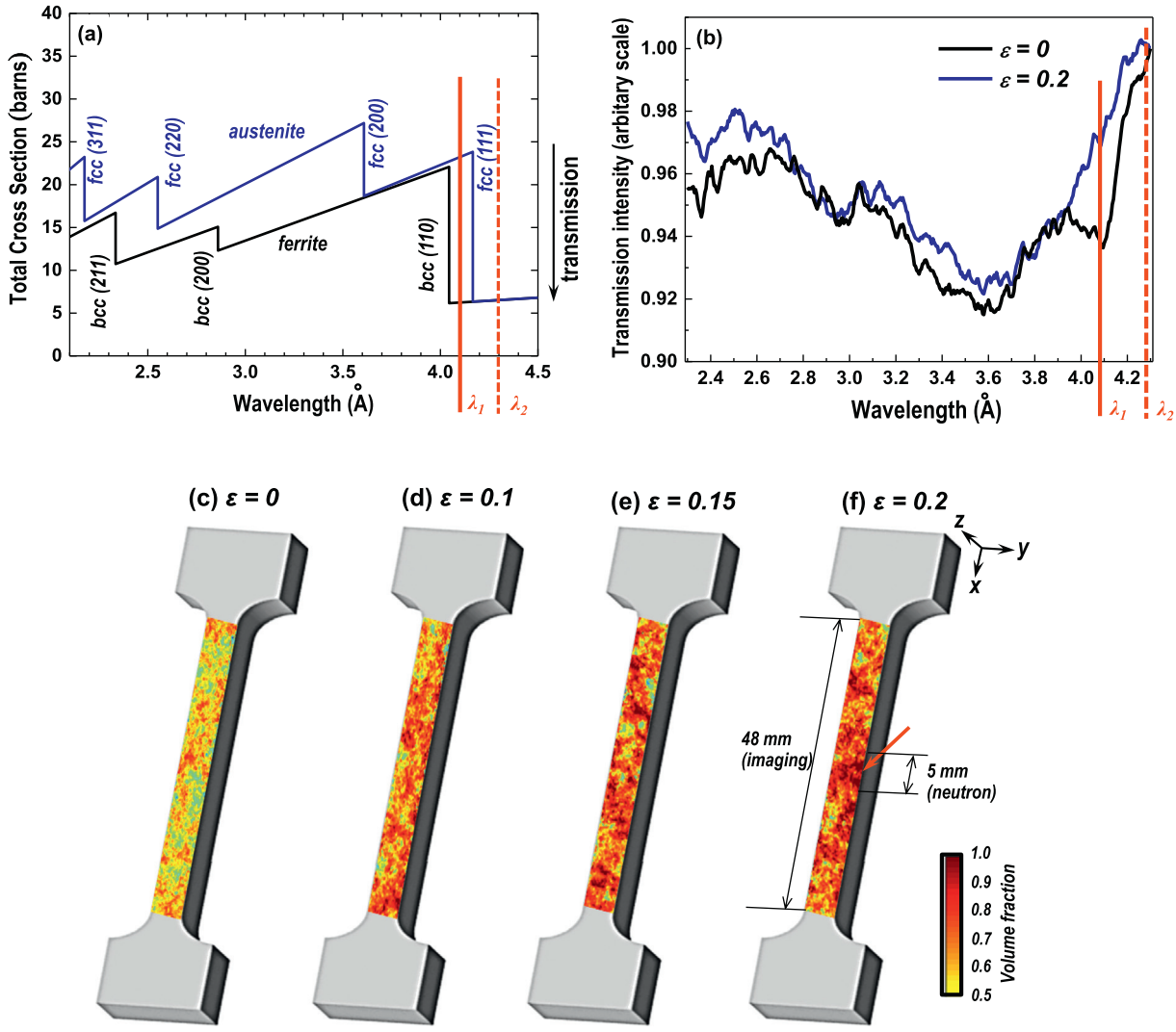

Fig. 3. (a) Total neutron cross section (σ) of the bcc ferrite and fcc austenite as a function of wavelength (λ). Marked indices (hkl) of several Bragg edges at the corresponding wavelengths. The marked λ_1 (4.1 Å) and λ_2 (4.3 Å) is the selected and background wavelength for current ESNI analysis, respectively, (b) transmission intensity variations as a function of λ when strain (ε) is 0 and 0.2, and two dimensional distribution of the volume fraction by ESNI as a function of ε; (c) 0, (d) 0.1, (e) 0.15, and (f) 0.2. Index is the volume fraction of bcc ferrite or bct martensite phases.

suggested. The volume fraction of each loading stage of a constituent phase, V_i^ε, can be described by $A_i^\varepsilon/A = (A_i^o + \Delta A_i^\varepsilon)/A$ $(i = \alpha, \gamma)$, where A is the total scan area of the EBSD and A_i^ε is the scan area of a phase at each strain stage. The A_i^ε is composed of the initial scan area (A_i^o) and changes of the scan area (ΔA_i^ε) at a strain stage of a constituent phase. Note that we adopt the A_i^o for the neutron diffraction results (i.e., 0.63 of $\alpha + \alpha'$ and 0.37 of γ, Table 1) and the ΔA_i^ε for the EBSD, Fig. 1. As a result, the volume fraction of the $EBSD^M$ is obviously comparable to the neutron and imaging results as shown in Fig. 4. This methodology can be applied for the prediction of the volume fractions using EBSD (ΔA_i^ε parts) combined with the initial value of the neutron diffraction.

Finally, let us discuss about the advantages of the ESNI method compared to the EBSD and in situ neutron diffraction. The ESNI can provide the volume fraction of a phase over the cm-scale from the entire specimen. For example, in the current study, the scan length was 4.8 cm, which is 100 times longer than EBSD as shown in Fig. 2(a). Furthermore, the deep penetration nature of neutrons can provide the spatial average through the thickness (e.g., 1.6 mm) of the specimen. Thus, it shows the two dimensional distributions of constituent phases with μm-scale spatial resolution (e.g., 65 μm). Fig. 3(f) shows that the martensite was concentrated on the necking region (marked with an arrow), where is known to be located near the center of the gauge parallel length during

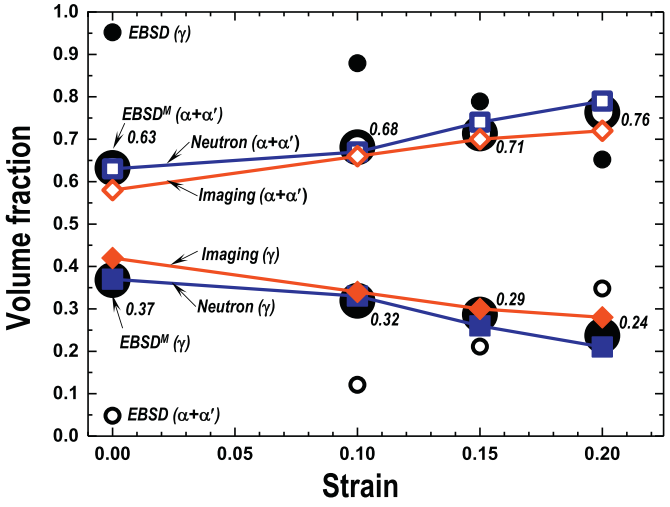

Fig. 4. Evolutions of the volume fraction of ferrite (α), martensite (α′), and austenite (γ) phases as s function of strain measured by EBSD, in situ neutron diffraction, and energy selective imaging methods. The marked values of $EBSD^M$ are a modified result combined between the neutron diffraction result for the initial fractions and EBSD values for the changes as straining.

plastic deformation in ductile metals [20]. The discrepancy of the martensite volume fraction between ESNI (0.14) and neutron diffraction (0.16) at $\varepsilon = 0.2$ in Table 1 is likely due to due to the higher volume fraction of α and α′ volume fraction in the necking region and the difference of averaging volume between neutron diffraction and ESNI as shown in Fig. 3(f).

In summary, the volume fractions of the constituent phases were determined as a function of strain (ε = 0, 0.1, 0.15, and 0.2) in a TRIP-assisted duplex stainless steel by using EBSD, in situ neutron diffraction, and ESNI methods. The imaging method utilized the transmission intensity difference at the Bragg edge between bcc (110) and fcc (111) using the selected wavelength (4.1 Å). It determines the volume fractions of the martensite and austenite through the thickness of the specimen along the cm-scale scanning coverage. More importantly, two dimensional distributions of constituent phases enable us to show the martensite distribution concentrated on the necking region of the tensile specimen with the 65 μm spatial resolution.

Acknowledgements

This work was supported by the National Research Foundation of Korea (NRF) grant funded by the Korean government (No. NRF-2017M2A2A6A05017653). Authors thank to TJ Kim, DK Kim, E Shin, and SW Lee.

References

[1] R.N. Gunn, Duplex Stainless Steels, Abington, Cambridge, 1997.
[2] J. Wang, P.J. Uggowitzer, R. Magdowski, M.O. Speidel, Scr. Mater. 40 (1999) 123.
[3] C. Herrera, D. Ponge, D. Raabe, Acta Mater. 59 (2011) 4653.
[4] T.-H. Lee, H.-Y. Ha, J.-Y. Kang, B. Hwang, W. Woo, E. Shin, Scr. Mater. 67 (2012) 141.
[5] J.Y. Choi, J.H. Ji, S.W. Hwang, K.-T. Park, Mater. Sci. Eng. R 50 (2012) 32.
[6] N. Tsuchida, T. Kawahata, E. Ishmaru, A. Takahashi, ISIJ Inter. 54 (2014) 1971.
[7] Y. Kim, Y.M. Kim, J.-Y. Koh, T.-H. Lee, W. Woo, H.N. Han, Scr. Mater. 119 (2016) 1.
[8] E.-Y. Kim, W. Woo, Y.-H. Heo, B.S. Senog, J.Y. Choi, S.-H. Choi, Int. J. Plast. 79 (2016) 48.
[9] Y. Zhao, W. Zhang, X. Liu, Z. Liu, G. Wang, Metall. Mater. Trans. A 47 (2016) 6292.
[10] Y. Li, W. Li, J.C. Hu, H.M. Song, X.J. Jin, Int. J. Plast. 88 (2017) 53.
[11] M. Moallemi, A. Zarei-Hanzaki, M. Eskandari, A. Burrows, H. Alimadadi, Metall. Mater. Trans. A 48 (2017) 3675.
[12] R. Woracek, D. Penumadu, N. Kardjilov, A. Hilger, M. Boin, J. Banhart, I. Manke, Adv. Mater. 26 (2014) 4069.
[13] J.R. Santisteban, L. Edwards, A. Steuwer, P.J. Withers, J. Appl. Crystallogr. 34 (2001) 289.
[14] W. Kockelmann, G. Frei, E.H. Lehmann, P. Vontobel, J.R. Santisteban, Nucl. Inst. Methods Phys. Res. A 578 (2007) 421.
[15] M. Schilz, P. Böni, E. Calzada, M. Mühlbauer, B. Schillinger, Nucl. Inst. Methods Phys. Res. A 605 (2009) 33.
[16] E.H. Lehmann, W. Wagner, Appl. Phys. A Mater. Sci. Process. 99 (2010) 627.
[17] N. Kardjilov, I. Manke, A. Hilger, M. Strobl, J. Banhart, Mater. Today 14 (2011) 248.
[18] R. Woracek, D. Penumadu, N. Kardjilov, A. Hilger, M. Strobl, R.C. Wimpory, I. Manke, J. Banhart, J. Appl. Phys. 109 (2011), 093506. .
[19] D.S. Hussey, I.C. Brocker, J.C. Cook, D.L. Jacobson, T.R. Gentile, W.C. Chen, E. Baltic, D.V. Baxter, J. Doskow, M. Arif, Phys. Procedia 69 (2015) 48.
[20] R. Woracek, D. Penumadu, N. Kardjilov, A. Hilger, M. Boin, J. Banhart, I. Manke, Phys. Procedia 69 (2015) 227.
[21] W. Woo, V.T. Em, E.-Y. Kim, S.H. Han, Y.S. Han, S.-H. Choi, Acta Mater. 60 (2012) 6972.
[22] G.E. Bacon, Ch. 4, Experimental Techniquies for Diffraction Measurements 1975, pp. 111–115.
[23] W. Woo, V.T. Em, B.S. Seong, E. Shin, P. Mikula, J. Joo, M.-H. Kang, J. Appl. Crystallogr. 44 (2011) 747.